processes

MDPI

Article

Structural Design and Preparation Process Research of Stacked MEMS Gas Sensors for Volatile Organic Compound Gases

Guizhou Wu [1], Junfeng Wu [1,*], Juan Dong [2] and Xinyu Zhang [3]

[1] School of Measurement and Communication Engineering, Harbin University of Science and Technology, Harbin 150080, China
[2] School of Electronics and Information Engineering, Nanjing University of Information Science and Technology, Nanjing 210044, China
[3] He Harbin Power Plant Valve Company Limited, Harbin 150000, China
* Correspondence: hlj_wujunfeng@163.com

Abstract: To design gas sensors with fast response speed and high sensitivity for the detection of volatile organic compounds, a stacked MEMS sensor was designed in this study. It utilizes porphyrin-sensitive materials and carbon nanotubes to form composite materials, improve the thermal stability of sensitive materials, and conduct sensor gas sensitivity testing. The results show that the design of the thermal insulation structure makes the sensor obtain lower power consumption and more uniform temperature distribution, and the maximum deformation variable is 3.7×10^{-2} μM. Doping carbon nanotubes in porphyrin-sensitive materials can effectively improve their thermal stability, and the sensor is in a safe state at temperatures below 358 °C. The sensor with higher response recovery characteristics at a low concentration of 80 ppm aniline has better response recovery characteristics, with a response time of 33 s and a recovery time of 23 s, respectively; its response recovery characteristics to 1% high concentration ethanol gas are good, with a recovery time of 13 s and a sensitivity of 1.05. In the analysis of the sensor image characteristics, when the Euclidean distance threshold is set to five, four gases such as aniline and formaldehyde can be classified. The sensor designed in this study can effectively detect four gases, including aniline and formaldehyde.

Keywords: volatile organic compounds; gas sensitivity characteristics; porphyrin zinc; MEMS gas sensor

Citation: Wu, G.; Wu, J.; Dong, J.; Zhang, X. Structural Design and Preparation Process Research of Stacked MEMS Gas Sensors for Volatile Organic Compound Gases. *Processes* **2023**, *11*, 2554. https://doi.org/10.3390/pr11092554

Academic Editors: Ming Kwang Tan and Narayanan Ramakrishnan

Received: 20 June 2023
Revised: 4 August 2023
Accepted: 14 August 2023
Published: 25 August 2023

1. Introduction

Volatile organic compounds (VOCs) are a class of organic compounds that are highly volatile at room temperature and pressure and have a pungent odor. VOCs tend to react with nitrogen oxides under the influence of ultraviolet radiation, resulting in the formation of air pollutants such as ozone and organic aerosols. This poses serious threats to the natural environment and human health [1–4]. How to accurately and efficiently detect VOC gas is a hot and difficult topic in current VOC gas research. Currently, the detection of VOC gas can be achieved through various sensor sensitive materials and detection principles, including metal oxide, organic semiconductor, electrochemical, optical sensors, etc. Metal oxides are currently the most widely used type of sensor, with advantages such as low cost, high sensitivity, and fast response. However, most metal oxides need to operate at higher temperatures and have sensitive responses to multi-component gases. Therefore, the selectivity of metal oxides is not high. In comparison, organic semiconductor gas sensors can exhibit good gas sensing performance at room temperature and even at low temperatures, and have good selectivity and broad application prospects. Micro-electro-mechanical systems (MEMS) sensors are widely used in fields such as chemical engineering [5–8]. Therefore, their application in VOC gas detection aims to improve the performance of gas sensors and effectively detect VOC gas by utilizing porphyrin-based materials with excellent optical properties in the fabrication of sensitive materials. This

research is divided into four parts. The first is a literature review, which introduces the research situation of domestic and foreign scholars on different types of VOC gas sensors, as well as MEMS sensors and porphyrin materials. The second focuses on the design and preparation of stacked MEMS gas sensors, introduces the preparation of porphyrin-sensitive materials, and tests the gas sensitivity of the sensors. The third conducts gas sensitivity tests on the prepared gas sensors and analyzes the performance of different porphyrin-sensitive materials. The fourth summarizes the purpose, methods, results, etc., of the research, and analyzes future research directions.

2. Related Work

The distribution of VOCs in the atmosphere can cause air pollution and affect people's health and well-being. Therefore, conducting VOC gas detection has important practical significance. Acharyya et al. conducted relevant measurements using chemical resistance sensors to address the issue of VOC gas recognition. The results show that the proposed method can selectively identify VOC gases and reduce the cross-sensitivity of the resistive gas sensor to a certain extent [9]. Fedorov et al. used electrochemical synthesis methods to fabricate gas sensors and conducted related tests. From the test results, it can be seen that at a temperature of 300 °C, when the gas sensor is in an environment with low ppm concentration of alcohol vapor mixed with air, its chemical resistance response is more significant [10]. Srinivasan et al. analyzed g-CN in chemical sensors in the field of sensor fabrication and explored its application research in sensing. They analyzed the sensing mechanism of g-CN and the relevant principles of selective detection, and pointed out its future development direction [11]. Xing et al. used nanocomposites in sensor fabrication and applied them to VOC gas detection, and conducted relevant gas tests through experiments. From the research results, it can be seen that the gas sensing performance of the produced sensor is good, and the reason for its good sensing performance is due to factors such as the special porous surface morphology and the strong catalytic ability of metallic silver [12]. Bouricha et al. faced the detection problem of formaldehyde and other gases, selected a single sensor, used porphyrin-zinc materials for dynamic response, and selected principal component analysis methods to conduct research. From the grouping experiment, it can be seen that the proposed method can classify different individual vapors and effectively identify different VOC gases [13].

Osawa et al. conducted research on the relationship between cardiovascular diseases and blood pressure pulse waves, combined with MEMS triaxial force sensors and other instruments to form related equipment, and used it to measure blood pressure and other related work. Through experiments, it is found that this method can detect the characteristics related to blood pressure, pulse wave, and electrocardiogram, and thus realize the diagnosis of cardiovascular diseases [14]. Liao introduced the progress in sensors, analyzed the latest developments in MEMS sensors, and examined the advantages of diamond in improving sensor performance. They also introduced the relevant application prospects [15]. Nuzzo et al. faced the aging problem of civil infrastructure equipment, and to monitor its damage, taking into account economic and safety considerations, wireless sensor nodes were used for relevant monitoring. During this period, MEMS accelerometers were designed. The experiment indicates that the proposed method has high measurement accuracy and high feasibility, and can reduce costs [16]. Burger et al. analyzed the relevant porphyrin metal-organic frameworks in their research on sensing materials and studied their related optical oxygen-sensing performance. The research indicates that when the sensing material is in a water environment, its oxygen sensitivity is weakened. The higher the temperature, the lower the corresponding quenching constant. The surface-adsorbed oxygen in the material is conducive to promoting the quenching process [17].

In summary, there are several types of VOC gas sensors, and although chemical sensors have a fast response time, their operation is relatively complex. For example, for electrochemical sensors, in their working principle, the target gas molecules in contact with the sensor first pass through a membrane that prevents condensation, and then the gas

molecules diffuse through the capillary tube, possibly through a subsequent filter, and then reach the surface of the sensing electrode through a hydrophobic membrane. There, the molecules are immediately oxidized or reduced, producing or consuming electrons and generating an electric current. This is the basis for gas detection. Organic semiconductor sensors can work at room temperature and have features such as low power consumption, low cost, and simple operation. With the development of MEMS technology, their fabrication methods will evolve toward miniaturization and have broad application prospects. Therefore, research has applied it to the fabrication of VOC gas sensors. In response to the good thermal stability of porphyrin-based organic materials, they are applied in the preparation of sensors.

3. Porphyrin-Based VOC Gas Sensor Based on MEMS

To detect VOC gas in a closed environment, research is conducted on the fabrication of relevant sensor micro hot plates in view of MEMS technology, to solve the problem of high power consumption of gas sensors. To enhance the gas-sensing properties of gas sensors, porphyrin-sensitive materials were prepared, and their initial resistance was improved by doping carbon nanotube materials. The research involves building a gas sensitivity testing platform, and conducting sensor gas sensitivity testing from two aspects, electrical and image characteristics, to achieve qualitative and quantitative detection of VOC gas [18].

3.1. Structural Design and Process Preparation of MEMS Sensors

Micro hotplates play an important role in MEMS sensors. Porphyrin-sensitive materials are coated on their signal electrodes, and after encapsulation, corresponding gas sensors can be obtained. The micro hot plate includes multiple components, such as heating electrodes, insulation layer, signal electrode plate, etc. The signal electrode plate can collect gas-sensitive signal changes, and the insulation layer has thermal conductivity. When a certain voltage is continuously applied to the micro hot plate, the heating electrode generates heat through the Joule heat effect of the metal. Through three heat transfer methods, namely, heat convection, heat conduction, and heat radiation, heat transfer is carried out between the layers of the micro hot plate, while heat loss is also generated, so that the whole micro hotplate is in a dynamic equilibrium state. On the one hand, at a certain operating temperature, the sensitive material on the upper layer of the micro hot plate will adsorb or desorb gas, and the resistance value of the micro hot plate will also change with the change of external gas concentration. In view of this characteristic, it can be used to detect gas concentration. In addition, due to the change of temperature, different parts of the micro hot plate undergo different expansions, resulting in thermal stress and deformation. The Fourier law formula for heat conduction is shown in Equation (1).

$$\frac{dQ}{dt} = -\lambda A \frac{dT}{dL} \tag{1}$$

Equation (1) sets the thermal conductivity of the material to λ, where λ is expressed in W/m·K, t represents time, and Q represents heat. The higher the λ value, the better the thermal conductivity. It represents the thermal conductivity area as A, expressed in square meters, where T represents temperature and L represents length. In thermal convection, the relevant formula is shown in Equation (2).

$$Q = h(Ts - Ta) \tag{2}$$

In Equation (2), it sets the convective heat transfer coefficient to h, expressed in W/(m^2 °C), and sets the temperature of the solid surface to Ts; around a solid, it represents its fluid temperature as Ta. In the design of MEMS micro hot plate, it adopts a layered structure, which includes multiple layers, including silicon substrate and SiO_2 insulation layer. The structural schematic diagram is shown in Figure 1.

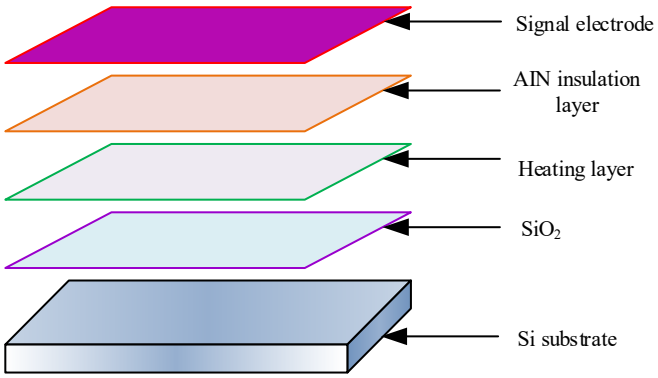

Figure 1. Schematic diagram of relevant structures.

In Figure 1, the framework of the MEMS micro hot plate is the substrate, which plays a supporting role in the structure. The substrate used is a monocrystalline silicon substrate. In different hierarchical structures, it designs heating electrodes and signal electrodes. By using a heating electrode, the gas sensor can obtain a suitable working temperature and check the resistance changes of sensitive materials through the signal electrode. To maintain the chemical and mechanical stability of the electrode at high temperatures, platinum is selected as the material for the heating electrode and signal electrode. The use of silica as an insulating layer has a lower thermal conductivity and can effectively reduce heat loss. The insulation thermal conductivity layer is a layer of AlN thin film, which has high thermal conductivity, good insulation, and strong adhesion. Under the action of AlN thin film, electrical insulation can be carried out, resulting in higher heat transfer efficiency between the two electrodes mentioned above. According to the actual size of 1:1, the three-dimensional geometric modeling of the micro hotplate is constructed. There are two types of structures; micro hot plate 1 is a diaphragm-type structure, and micro hot plate 2 is a suspended structure, as shown in Figure 2.

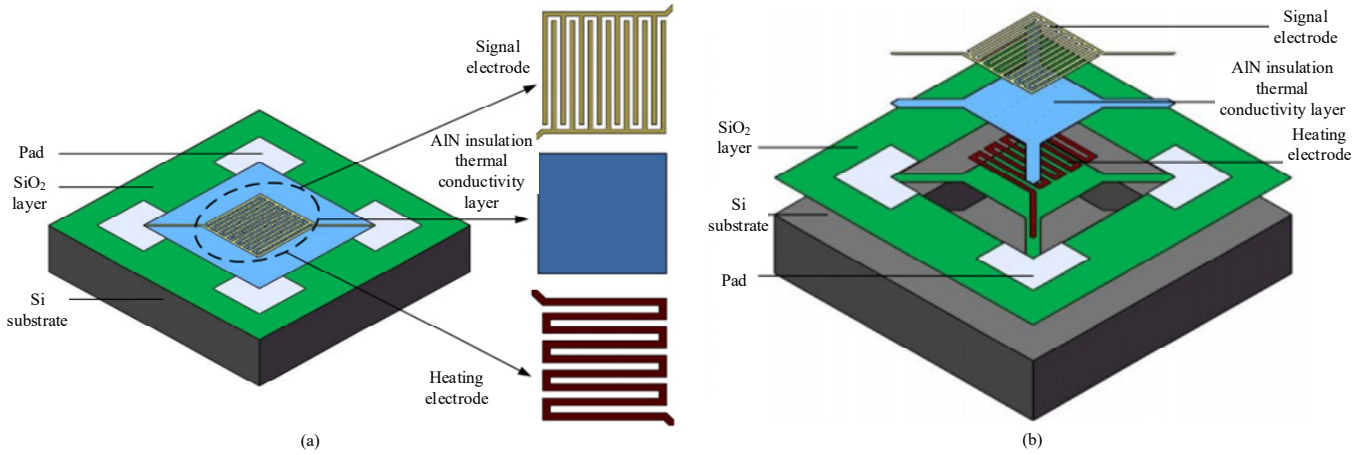

Figure 2. Structure of two types of micro hot plates. (**a**) Structure of Micro Hot Plate 1. (**b**) Structure of Micro Hot Plate 2.

In Figure 2a, within the active region, the heating electrode is connected to the signal electrode and there is contact, which makes the structure more stable. In Figure 2b, the active area is processed by hollowing out the surrounding area, and the middle active area is supported by several cantilever beams, making the entire active area suspended; by thinning the back, the heat transfer channel is cut off to reduce heat loss. The shape and size of the electrodes in the two structures of the micro hot plate are the same, with the size of the micro hot plate being 1 mm × 1 mm × 0.3 mm, which is smaller than the volume of traditional sensors. The line width, spacing, and thickness of the signal electrode are 10 μm,

10 μm, 0.2 μm, respectively; AlN size is 300 μm × 300 μm, with a thickness of 0.2 μm. For heating electrodes, their line width, spacing, and thickness are, respectively, 15 μm, 15 μm, 0.2 μm. For the silicon dioxide, its size is 1 mm × 1 mm with a thickness of 0.5 μm. For silicon substrates, their size is 1 mm × 1 mm, with a thickness of 300 μm.

By using ANSYS10.0 finite element simulation software, it is possible to analyze the steady-state thermal and thermal stress of the micro hot plate. Using the form of grid division, the structure is processed to obtain numerical values for each small region, thus approximating the entire structure. Before conducting simulation analysis, make relevant assumptions. In the heat transfer of the micro hot plates, the influence of thermal radiation is ignored. It takes the thermal conductivity of each material in the micro hot plate as a constant. The external conditions do not affect the heating of the electrode resistance, and the heat generation rate is constant; in the micro hot plate, the materials with different structures are tightly connected without gaps. During the thermal convection process between the micro hot plate and the air, the thermal convection coefficient is 25 W/(m^2 °C) and the ambient temperature is 22 °C.

During simulation, it models the micro hot plate, sets material parameters, divides the mesh, applies boundary conditions and loads, and performs relevant calculations. The relevant material parameters are shown in Table 1.

Table 1. Material Parameters.

Materials and Parameters	Substrate	Insulation Layer	Electrode	Insulation and Thermal Conductivity Layer
Material	Si	SiO_2	Pt	AlN
Thermal conductivity coefficient (W/m·k)	1.57	1.4	73	180
Elastic modulus (GPa)	190	73	169	310
Poisson's ratio	0.23	0.16	0.38	0.20
Thermal expansion coefficient (1/°C)	2.6×10^{-6}	0.5×10^{-6}	8.9×10^{-6}	4.2×10^{-6}

In Table 1, the corresponding coefficient of thermal expansion varies with the materials of different parts. After the conducting simulation analysis, the appropriate micro hot plate is selected. On this basis, the manufacturing process of MEMS micro hot plate is studied, and the relevant process is shown in Figure 3.

In Figure 3, LPCVD stands for low-pressure chemical vapor deposition, CMP represents chemical mechanical polishing, and ICP represents inductively coupled plasma. In fabrication, it first chooses double-sided polished silicon wafers with a thickness of 300 μm. The crystal surface is <100>, which is cleaned sequentially with acetone, anhydrous ethanol, and deionized water in an ultrasonic cleaning machine at a frequency of 40 kHz, each time for 15 min, and then dried. It prepares an SiO_2 insulation layer, double-sided preparation of 500 nm SiO_2 through LPCVD, and CMP treatment to make the surface of the obtained SiO_2 film flat. In the production of heating electrodes, the Pt heating electrode is first produced by the lift-off stripping process. At a speed of 3000–5000 rpm, the homogenizer applies AZ5214 photoresist above the SiO_2 layer on the silicon substrate, with a thickness of about 2 μm. The silicon wafer is placed in a vacuum-drying oven and dried at 95 °C. Subsequently, customs clearance, development, sputtering of Pt film, and lift-off stripping were performed to obtain the prepared heating electrode. AlN thin films with a thickness of 500 nm were deposited on the silicon substrate by magnetron sputtering. CMP treatment, coating, exposure, development, and other steps are carried out to obtain the final AlN thin films. The signal electrode pattern is selected and a mask is fabricated. By repeating steps such as uniform glue and exposure, the Pt film is deposited on the front of the silicon wafer with a thickness of 200 nm. Under the action of lift-off stripping technology, the signal electrode pattern is obtained and subjected to wet degumming and cleaning treatment. It is used to prepare an isolation structure and thin the back of the silicon substrate. Through

steps such as homogenization and ICP etching, a silicon structure with reduced back thickness is obtained. It performs etching treatment on the upper isolation structure, follows the mask pattern, and undergoes gluing, exposure, and development, in a top-down order. By using the ICP etching method, the SiO_2/Si structure on the top layer of the chip is etched, followed by wet degumming, cleaning, drying, and laser scribing to obtain an independent unit of MEMS micro hot plate with a size of 1 mm × 1 mm × 0.3 mm.

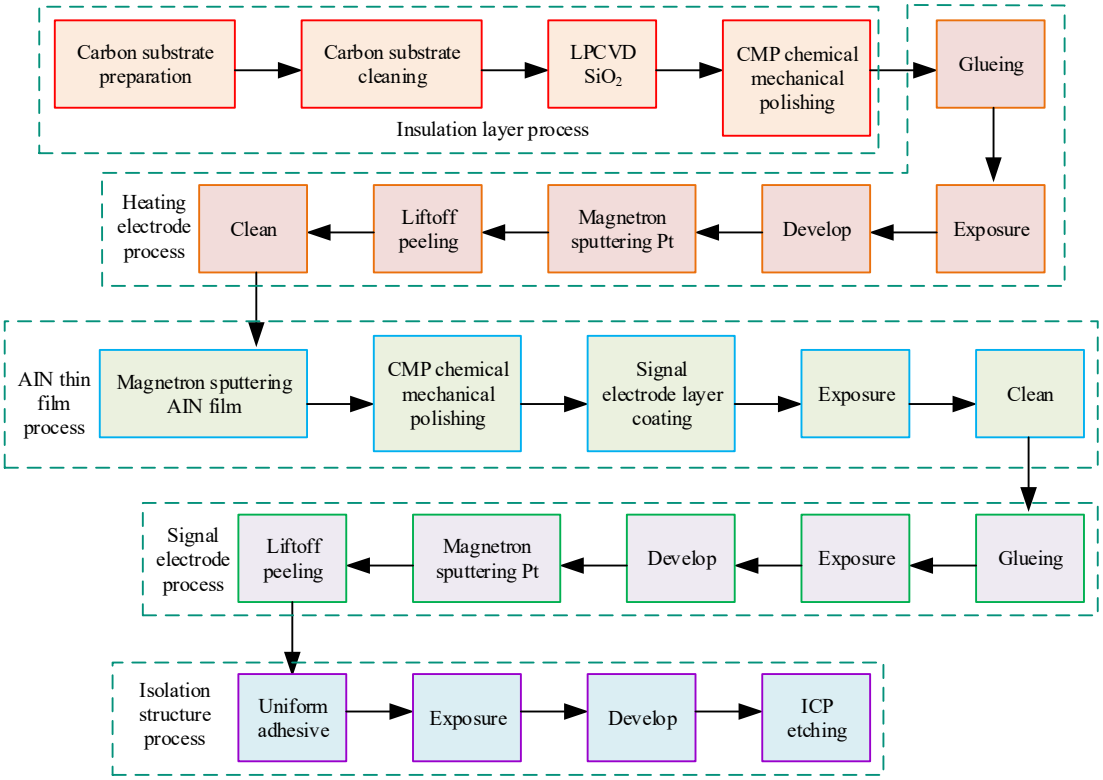

Figure 3. Related preparation process flow.

3.2. Preparation and Characterization of Porphyrin Sensitive Materials

To improve the gas-sensing characteristics of gas sensors, porphyrin-sensitive materials were prepared by doping carbon nanotube materials to improve their initial resistance values [19,20]. During this period, various instruments were applied, such as digital constant-temperature multihead magnetic stirrers, tabletop high-speed centrifuges, differential thermal gravimetric analyzers, etc. The reagents used are shown in Table 2.

Table 2. Related Reagents.

Serial Number	Drug Name	Specifications
1	Pyrrole (C_4H_5N)	98%
2	Benzaldehyde (C_7H_6O)	Analytical pure
3	Xylene (C_8H_{10})	Analytical pure
4	Salicylic acid ($C_7H_6O_3$)	98%
5	Anhydrous ethanol (C_2H_6O)	Analytical pure
6	N-N dimethylformamide (DMF)	Analytical pure
7	Zinc Acetate $Zn(C_2H_3O_2)_2{\cdot}2H_2O$	Analytical pure
8	Terpineol	Analytical pure
9	Multi walled carbon nanotubes	Chemically pure

In Table 2, different drugs have different specifications, and these reagents can be used to prepare porphyrin and porphyrin-zinc sensitive materials. Firstly, tetraphenylporphyrin

was synthesized using the Adler method. First, a 250 mL three-necked bottle is selected and salicylic acid and benzaldehyde are added to it with a mass ratio of 1:2. Then, 150 mL of xylene is added to the bottle for dissolution and magnetic stirring. After starting the reflux reaction in the condensation tube, the mixture of pyrrole and xylene should be added dropwise within 10 min. The pale yellow solution in the bottle will turn purple-black. After the reflux time of 180 min, the solution is no longer heated and is allowed to cool. When the temperature of the solution is about 25 °C, add 20 mL of anhydrous ethanol and allow to stand for 24 h. It is cleaned with anhydrous ethanol and filtered with a sand-core funnel. After filtration, it is dried for 6 h in a vacuum drying oven at a temperature of 90 °C to obtain a deep purple powder. The process used for the synthesis of tetraphenylporphyrin zinc is shown in Figure 4.

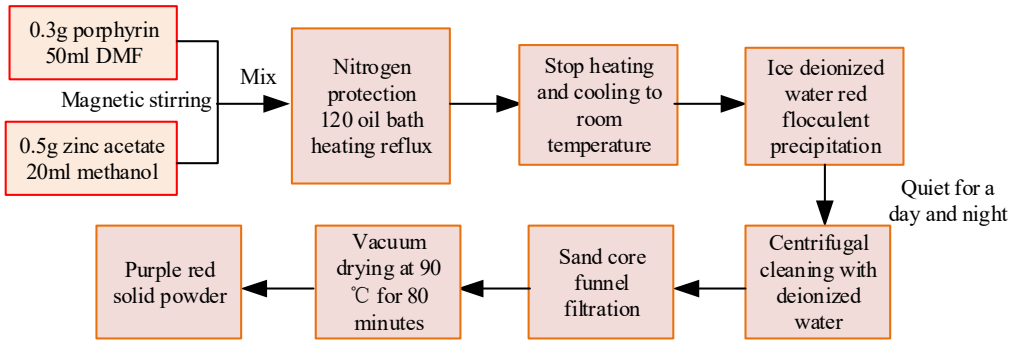

Figure 4. Related preparation process.

In Figure 4, the tetraphenylporphyrin powder was weighed using an electronic balance at a dose of 0.3 g. It is then poured into 50 mL of DMF for dissolution, and magnetic stirring is performed with a magnetic stirrer for 30 min to promote complete dissolution. Zinc acetate is weighed at 0.5 g and dissolved in 20 mL of methanol solution. It is thoroughly stirred under the action of a magnetic stirrer for 30 min. Tetraphenylporphyrin solution and zinc acetate solution are poured into a 250 mL three-necked bottle, the reflux condenser tube is connected, and N_2 is introduced to provide protection. Subsequently, it is heated using an oil bath heating method at 120 °C. Under the action of a magnetic stirrer, it is stirred thoroughly for 90 min and heating is stopped, resulting in a purple-red product. It is then cooled to about 25 °C. By adding 150 mL of deionized ice water, the solution precipitates red flocculent precipitates. After standing for a day and night, the precipitates separate from the upper liquid and the upper liquid is removed; under the action of deionized water and ethanol, centrifugal cleaning and precipitation were carried out at a speed of 4000 r/min for 10 min, repeated three times, to remove the residue of DMF and zinc acetate. It is subjected to suction filtration using a sand core funnel to obtain tetraphenylporphyrin zinc solid powder, which is then subjected to vacuum drying treatment for 80 min.

Due to the high resistance and poor conductivity of the obtained porphyrin zinc material, its application in electrical sensors will be affected. In addition, carbon nanotubes have good conductivity and optical properties and good stability, and can improve the performance of the material. Therefore, it is applied to the porphyrin zinc sensitive material to obtain a porphyrin zinc/carbon nanotube composite material, to reduce the initial resistance value of the porphyrin zinc sensitive material. During the doping process, the powder of carbon nanotubes and porphyrin zinc was selected by different mass ratios, and put into an agate mortar for mixing. Terpineol was added to bond the mixed powder, and it was thoroughly ground for 3 h. Then, it is coated on the interdigital electrode and subjected to vacuum drying at a temperature of 120 °C for 2 h to obtain the relevant gas sensor. The resistance values of these sensors are measured to obtain their initial resistance values in clean air. On this basis, combined with the gas-sensitivity testing of relevant sensors, the sensitivity of carbon nanotubes doped with different ratios to 50 ppm aniline was analyzed, and the optimal doping ratio of 7% was obtained from the obtained results.

Carbon nanotubes were used as dopants and doped in porphyrin zinc materials. The thermal stability of porphyrin materials is analyzed and differential thermal gravimetric tests are performed using a ZCT-B differential thermal gravimetric analyzer [21].

3.3. Sensor Gas-Sensing Testing Platform Based on Electrical Gas-Sensing Performance and Image Gas-Sensing Performance

The MEMS sensor chip and porphyrin-sensitive materials obtained from the above preparation are used to fabricate MEMS gas sensor units. The gas-sensing performance of MEMS gas sensors is tested from two aspects: electrical gas-sensing performance and image gas-sensing performance. First, a sensing platform is constructed and a sensor unit is fabricated. Then, carbon nanotubes are doped with porphyrin zinc. The optimal doping ratio is selected to be 7%; they are mixed in an agate mortar, 1% trace H_2PtCl_6 and terpineol are added, they are mechanically ground for 3 h, the ground materials are coated on the signal electrode of the MEMS micro hotplate under an electron microscope, they are dried in a dark place for 24 h, and they are dried in a vacuum drying oven at 120 °C for 2 h to prepare MEMS gas sensors. By utilizing the catalytic effect of H_2PtCl_6, the adsorption and desorption processes of gas and composite gas-sensing materials are accelerated, resulting in higher gas-sensing performance of the materials. Among them, the sensitive materials used in the research institute have good conductivity, high thermal stability, and good uniformity. Through Altium Designer 17.1 software, the four array PCB sensor adapter board is drawn, and MEMS sensor chips are integrated on it. The chips coated with sensitive materials are fixed at four positions on the circuit adapter board, namely, A1, A2, B1, and B2, to obtain the corresponding four-array gas sensors. These sensors can simultaneously collect data, resulting in higher integration of gas sensors. In the construction of the detection platform, a gas reaction box is selected, which mainly consists of three parts: a base, a movable body, and a top cover. There is a circular hole in the middle of the top cover, where a microscope lens is placed to collect image signals. It utilizes the grooves on the four walls of the base to place the moving body, and by adjusting the moving body, the height of the detection device is changed. The four-array PCB sensor adapter board and the entire testing platform are shown in Figure 5.

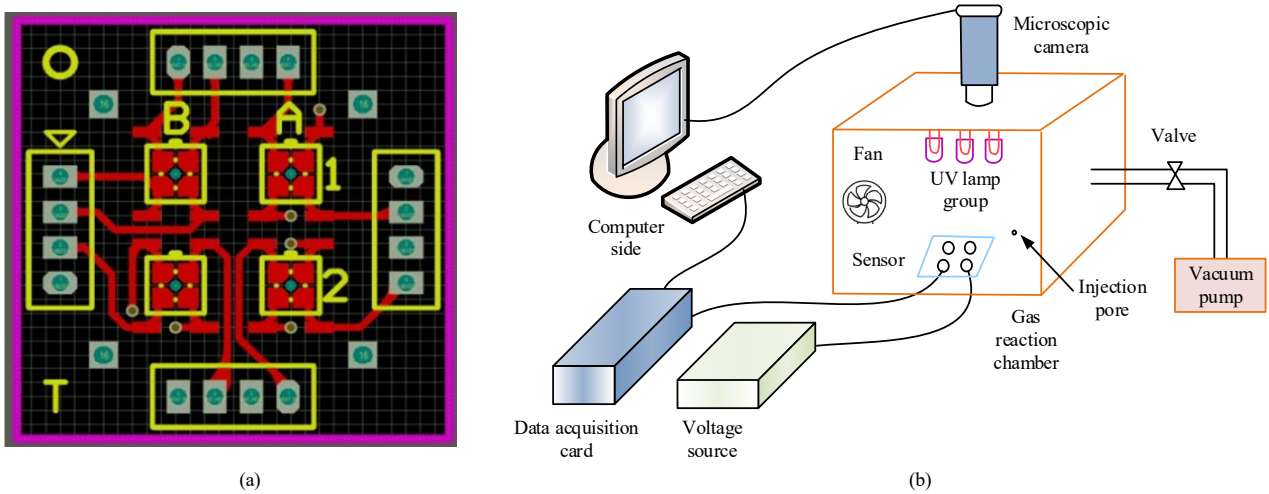

Figure 5. Schematic diagram of testing platform. (**a**) Quad array PCB sensor adapter board. (**b**) Schematic diagram of testing platform.

In Figure 5a, based on the letters and numbers marked, it can be seen that A1, A2, B1, and B2 are located. In Figure 5b, electrical and image signals can be collected through this test platform. The electrical signal acquisition section includes multiple parts, such as sensor arrays, voltage sources, etc. Through a data acquisition card, the resistance value of the sensor unit can be collected in real time. The image signal acquisition section includes sensor arrays, micro cameras, and other parts. The excitation light source required

by the sensor comes from the ultraviolet excitation lamp. After the testing platform is connected, the gas reaction chamber is sealed and processed. The vacuum pump in the ventilation system is used to timely remove the tested gas and prevent the accumulation of toxic gases. The testing conditions are the same, and the prepared MEMS gas sensor is tested. First, its electrical gas sensitivity performance is tested, including response recovery characteristics, gas sensitivity, repeatability, etc. The gas sensitivity calculation formula is shown in Equation (3).

$$S = Rg/Ra \tag{3}$$

In Equation (3), for the gas sensor, set its resistance value in the measured VOC gas to Rg, and represent its resistance value in air as Ra. For porphyrin-based sensors, porphyrins have a π electron system. When porphyrin materials come into contact with VOCs gas, there will be a significant interaction force between the molecules corresponding to the two substances, leading to physical adsorption, which can be realized in the form of Equation (4).

$$O_2 \rightarrow O_2(ads) \tag{4}$$

In Equation (4), O_2 represents oxygen molecules in the air, and $O_2(ads)$ represents oxygen molecules adsorbed on the surface of porphyrin-like materials. $O_2(ads)$ will combine with the surface electron e^- of the porphyrin to obtain $O^-{}_2$ as shown in Equation (5).

$$e^- + O_2(ads) \rightarrow O^-{}_2(ads) \tag{5}$$

In Equation (5), $O^-{}_2$ represents the adsorbed oxygen molecules after obtaining e^-. On this basis, combine e^- again to obtain the relevant expression as shown in Equation (6).

$$e^- + O^-{}_2(ads) \rightarrow 2O^-(ads) \tag{6}$$

In Equation (6), O^- represents the adsorbed $O^-{}_2$ after obtaining e^-. It is combined with e^- again to obtain the relevant expression as shown in Equation (7).

$$e^- + 2O^-(ads) \rightarrow O^{2-}(ads) \tag{7}$$

In Equation (7), O^{2-} represents the adsorbed O^- after obtaining e^-. When in contact with gases such as ethanol, ethanol will react with the adsorbed oxygen on the surface of porphyrin materials. The former will be adsorbed and oxidized, causing oxygen atoms to release electrons, which will appear in the conduction band on the surface of semiconductor porphyrin materials. The relevant expressions are shown in Equations (8) and (9).

$$CH_3CH_2OH(ads) + 6O^-(ads) \rightarrow 2CO_2(g) + 3H_2O(l) + 6e^- \tag{8}$$

$$CH_3CH_2OH(ads) + 6O^{2-}(ads) \rightarrow 2CO_2(g) + 3H_2O(l) + 12e^- \tag{9}$$

In metalloporphyrins, both the central metal and π electron system can affect their gas-sensing performance; The higher the number of central metal electrons is, the higher the corresponding electron donating capacity is. The change of electron cloud density will lead to the change of porphyrin adsorption. Analyzing the sensor performance from the perspective of image gas-sensing performance, VOC gases include toluene, formaldehyde, ethanol, and aniline. After the porphyrin material comes into contact with VOC gas, its color will change. In view of this characteristic, the sensor gas sensitivity test is performed. Before testing, it turns on the ultraviolet lamp set with a wavelength of 365 nm, which emits fluorescence from the gas sensing array for a duration of 5 min; When the sensor is in a stable state, the pre reaction image of the porphyrin sensor can be obtained by taking photos with a micro camera. After the fan is turned on, it injects a certain concentration of the gas to be measured into the reaction chamber, contacts the sensor array, and fully reacts. After lasting for 10 min, it takes photos to obtain the image of the sensor's response.

It opens the vacuum pump valve to exhaust the gas inside the box, and the gas test is completed. If another experiment is to be conducted, these steps can be repeated. In units A1, A2, B1, and B2, relevant sensitive materials are coated, respectively. The materials of the first two units are porphyrin and porphyrin-zinc, while the materials of the last two units are porphyrin zinc/carbon nanotube composites and porphyrin-zinc/carbon nanotube composites with chloroplatinic acid added. It detects toluene, formaldehyde, aniline, and ethanol separately through these units.

Before and after ventilation, the color of the sensitive materials of the relevant sensors will change. Image processing technology is used for relevant processing analysis, and the relevant process is shown in Figure 6.

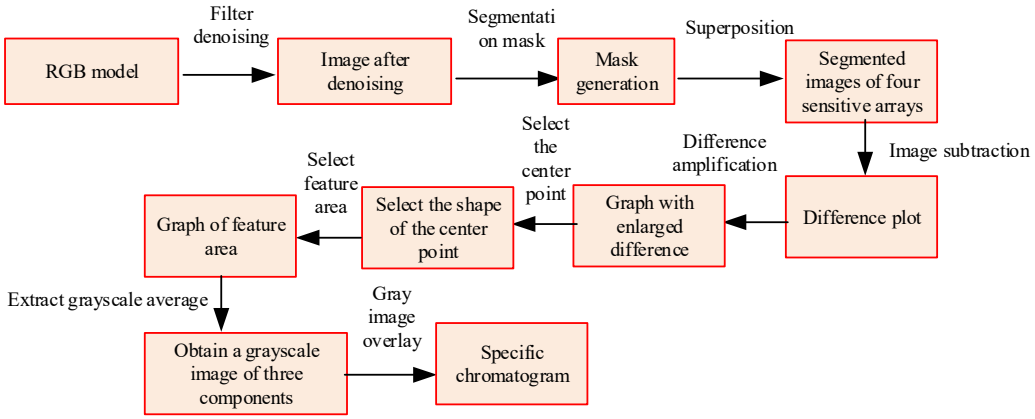

Figure 6. Sensor image processing process.

In Figure 6, due to the large amount of information present in each image, only key information is extracted. The pixel values of sensitive materials in the red green blue (RGB) channel and the coordinates of different pixel positions are extracted. It represents the pixel values of the color image by a 2 × 2 four-array image, selecting a position at the center of the sensor unit. The color model is an RGB color model, which is denoised by the Gaussian filter denoising algorithm in Matalab. After the processing is completed, the image is binarized using the maximum variance between classes method. In the principle of this method, it assumes that the background of image I is relatively dark, the foreground and background style thresholds are T', and the image size is $M \times N$. In I, if the number of pixels with a grayscale value less than T' is N_0, the calculation formula for the proportion ω_0 of foreground pixels in the image is shown in Equation (10).

$$\omega_0 = \frac{N_0}{M \times N} \tag{10}$$

The formula for calculating the proportion ω_1 of background pixels to the image is shown in Equation (11).

$$\omega_1 = \frac{N_1}{M \times N} \tag{11}$$

In Equation (11), N_1 represents the number of pixels in I with grayscale values greater than T'. The relationship between ω_1 and ω_0 is shown in Equation (12).

$$\omega_1 + \omega_0 = 1 \tag{12}$$

$N_0 + N_1 = M \times N$, it sets the total average grayscale of the image to μ, and the calculation formula is shown in Equation (13).

$$\mu = \omega_0 \mu_0 + \omega_1 \mu_1 \tag{13}$$

In Equation (13), μ_1 represents the average grayscale of the image. The inter class variance is set to g, and its expression is shown in Equation (14).

$$g = \omega_0(\mu_0 - \mu)^2 + \omega_1(\mu_1 - \mu)^2 \quad (14)$$

It replaces Equation (13) into Equation (14) to obtain equation (15).

$$g = \omega_0\omega_1(\mu_0 - \mu_1)^2 \quad (15)$$

It solves to T' in view of the traversal method, obtains the binarization threshold of the image, generates a mask in view of this threshold, and overlays it with the filtered image. It extracts the sensitive material area of the sensor unit from the background and obtains the corresponding segmented image. It subtracts the images before and after the segmentation reaction to obtain the corresponding difference. Under the action of linear transformation, by amplifying the difference, it can be seen that the shape of the relevant sensitive material area is approximately circular. By using the first-order distance, the original center of gravity is calculated as the corresponding sensitive material center, and the center point graph is selected to obtain a 14 × 14 pixel square. The center of the circle is the center of gravity, and the square is used as the feature area. It extracts the average grayscale value and obtain the grayscale image of R, G, and B components. Among them, B represents the blue channel, while B1 and B2 represent the fixed position of the sensor chip on the circuit adapter board. Superposition the grayscale value images of the three components obtained to obtain the difference feature map of the sensitive material before and after the reaction with the gas to be tested. According to this processing method, it analyzes the changes in different components of VOC gas. In view of the feature vectors obtained from different VOC gases, a hierarchical clustering analysis is performed using the minimum variance clustering algorithm, and the similarity of the feature vectors is measured using the Euclidean distance.

4. Testing and Analysis of Porphyrin-Based VOC Gas Sensors Based on MEMS

It tests the prepared sensor chip and analyzes its performance through finite element simulation analysis. It characterizes and analyzes the porphyrin materials to study their thermal stability. It conducts sensor gas sensitivity tests from two aspects: the electrical and image characteristics of the sensor.

4.1. Simulation Analysis of Micro Hot Plate Structure and Characterization Analysis of Porphyrin Materials

The steady-state heat of the designed micro hotplate is simulated and analyzed, and the transverse temperature distribution of different micro hotplates can be obtained, as shown in Figure 7.

Figure 7a shows the variation of lateral temperature distribution of micro hotplate 1; Figure 7b shows the variation of lateral temperature distribution of micro hotplate 2. In Figure 7a, as a whole, the temperature of micro hot plate 1 first increases and then slowly decreases with increasing length. Among them, the temperature in the central active area is relatively low, with a large temperature difference of 4.632 °C, while the temperature outside the active area is lower. For micro hot plate 1, when its length is 0.2 mm, the corresponding temperature is 23.11 °C, which is 0.61 °C higher than when its length is 0.1 mm. When the length is 0.5 mm, the corresponding maximum temperature is 30.92 °C, while the transverse temperature is 29.24 °C when the length is 0.5 mm. In Figure 7b, the temperature of the active area of the micro hot plate 2 is mostly around 102 °C, with little temperature fluctuation and small temperature difference. In this area, the difference between the highest and lowest temperatures is 2.21 °C. Under the misuse of the thermal isolation structure design, the temperature distribution in the active area of the micro hotplate 2 is more uniform, and the temperature is higher than that of the micro hotplate 1, with lower heating power consumption. By analyzing the thermal stress

distribution and deformation distribution of micro hot plate 2, it was found that it bears a maximum stress of 0.1741 GPa and generates relatively small stress. The deformation area is mainly around the central active area, with a maximum deformation variable of 3.7×10^{-2} μm. The impact on micro hot plate 2 is relatively small. Therefore, micro hotplate 2 was selected for the study. The thermal stability of porphyrin materials was analyzed using the ZCT-B differential thermal gravimetric analyzer, and the relevant results are shown in Figure 8.

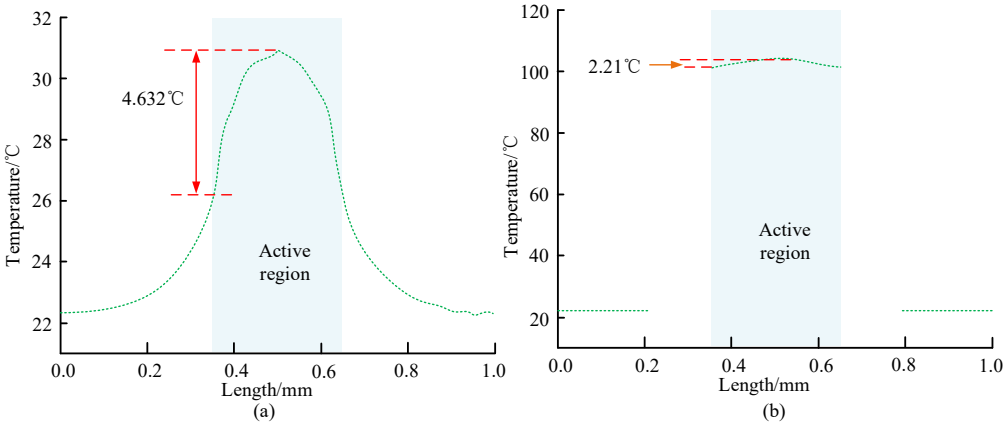

Figure 7. Transverse temperature distribution of micro hot plate 1 and micro hot plate 2. (**a**) Transverse temperature distribution curve of micro hotplate 1. (**b**) Transverse temperature distribution curve of micro hotplate 2.

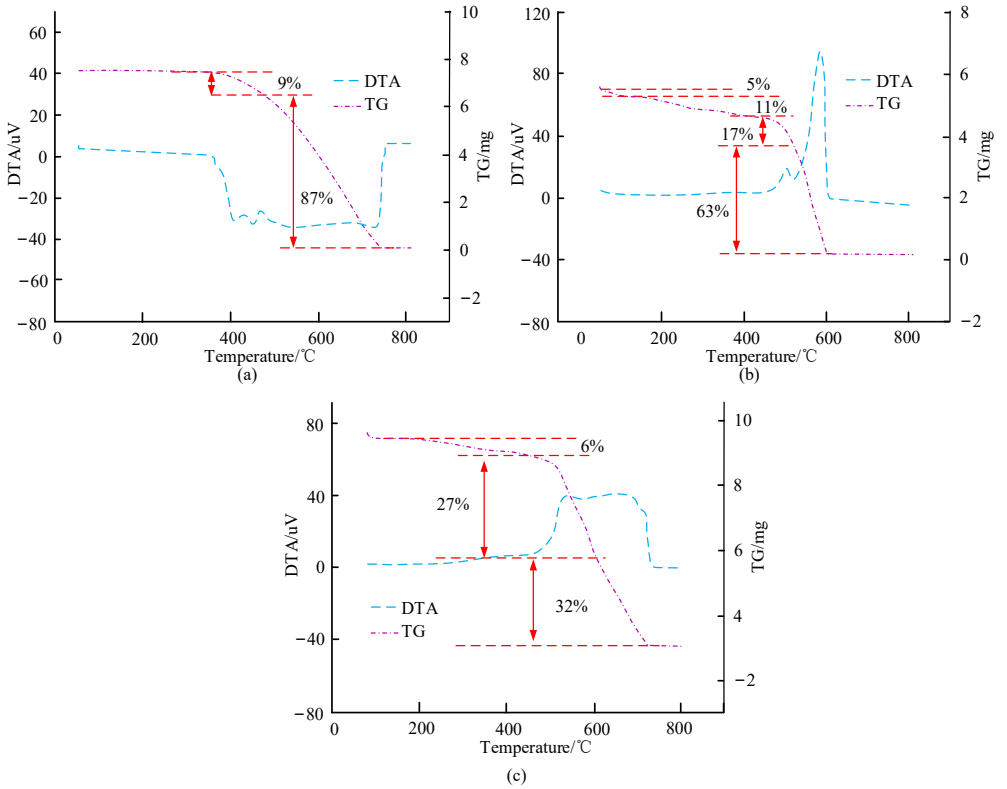

Figure 8. Differential thermal gravimetric analysis of related materials. (**a**) Differential thermal gravimetric analysis of porphyrins. (**b**) Differential thermal gravimetric analysis of zinc porphyrin. (**c**) Differential thermal gravimetric analysis of porphyrin zinc/carbon nanotube composite material.

In Figure 8, different porphyrin materials exhibit different differential thermal gravimetric curves. TG represents the thermogravimetric curve; DTA represents the differential

thermal curve. In Figure 8a, before 358 °C, the weight of the porphyrin material remained basically unchanged. It began to absorb heat from 358 °C, and there were two endothermic peaks between 358 and 467 °C, with a weight loss of about 9%. With continuous heat absorption, the quality of porphyrins will continue to decrease, and the weight loss rate will continue to increase. At about 731 °C, the porphyrins are completely decomposed. In Figure 8b, the weight loss rate of porphyrin zinc material is relatively slow, with a weight loss of 5% before 171.7 °C; Between 445.1 and 519.8 °C, there is an exothermic peak with a weight loss of 17%; The second exothermic peak is between 519.8 and 609.7 °C, with a weight loss of 63%; The temperature for complete decomposition of porphyrin zinc is 609.7 °C. In Figure 8c, before 464.4 °C, the weight loss of porphyrin zinc/carbon nanocomposites is 6%. In the curve, there are two exothermic peaks with symmetrical relationships, corresponding to temperatures of 542.9 °C and 694.2 °C, respectively. This demonstrates that the thermal stability of porphyrin zinc/carbon nanocomposites is good, and the corresponding sensor is in a safe state at temperatures below 358 °C.

4.2. Testing and Analysis of Sensor Gas Sensitivity Performance

It analyzes the gas sensitivity performance of the designed sensor and detects VOC gas. It studies the response recovery characteristics of the sensor after contact with the measured VOC gas. Taking aniline gas with a concentration of 50 ppm and ethanol gas with a concentration of 1% as examples, the corresponding results are shown in Figure 9.

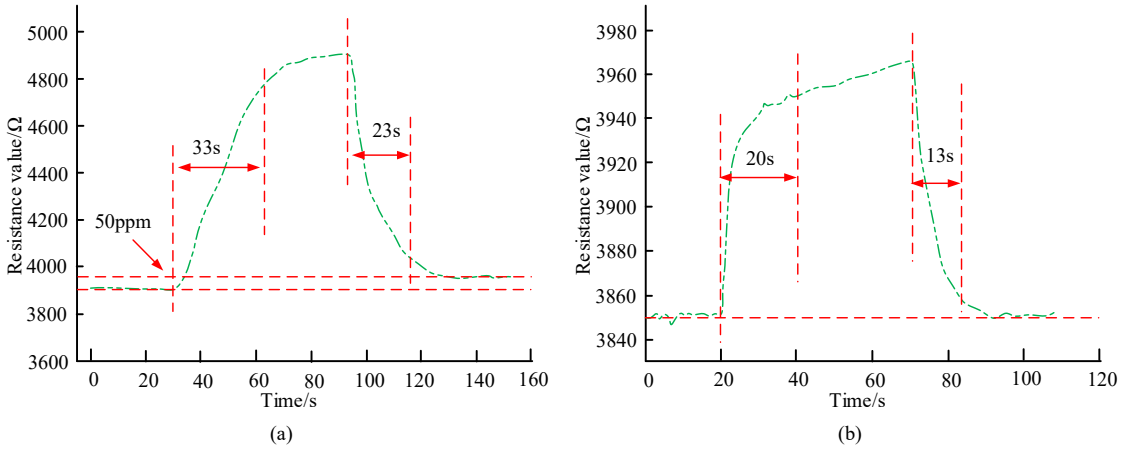

Figure 9. Response recovery characteristic curve of the sensor to 50 ppm aniline and 1% ethanol. (**a**) Response Recovery Characteristic Curve of Sensors to 50 ppm Aniline. (**b**) Response recovery characteristic curve of the sensor to 1% ethanol.

In Figure 9a, as the time increases, the sensor resistance first changes very little, then gradually increases, and then gradually decreases until it stabilizes and remains unchanged. The response time and recovery time of the aniline gas sensor are 33 s and 23 s, respectively. When the time is 60 s, the sensor resistance value is 4726 Ω, which is 17 Ω less than when the time is 100 s. The latter has a resistance value of 4743 Ω. After the gas is released, when the sensor resistance stabilizes, the final resistance value is slightly higher than the initial resistance value. In Figure 9b, as time increases, the sensor resistance first changes very little, then gradually increases, and then gradually decreases until it stabilizes and remains unchanged. The response time of the ethanol sensor is 20 s, and the recovery time is 13 s. The former is 10 s longer than the latter. After the gas is released, the resistance value of the sensor can be restored to the value before the reaction. It reveals that the sensor designed in the study has good response and recovery characteristics for VOC gas. The sensitivity of the analysis sensor in different concentrations of aniline gas and ethanol gas is shown in Figure 10.

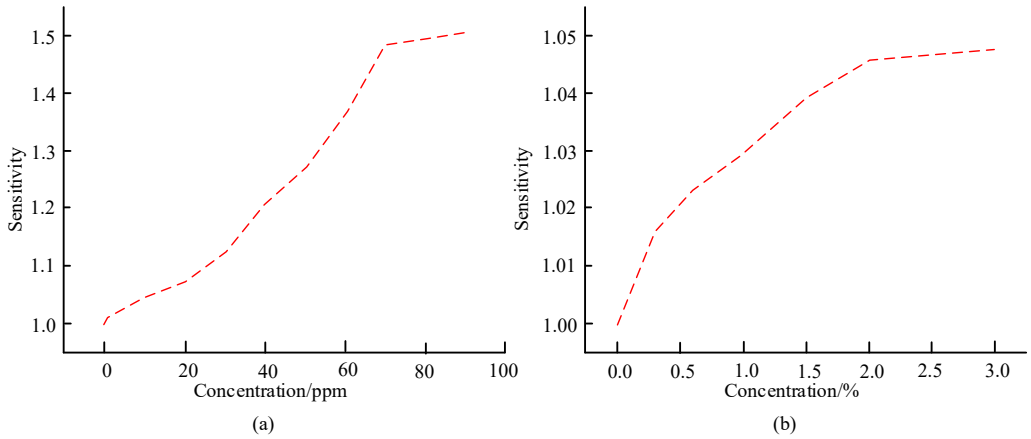

Figure 10. Sensitivity of sensors to different concentrations of aniline gas and ethanol gas. (**a**) Sensitivity of sensors to different concentrations of aniline gas. (**b**) Sensitivity of sensors to ethanol gas of different concentrations.

In Figure 10a, the sensitivity of the sensor shows an overall increasing trend as the concentration of aniline gas increases. When the concentration of aniline gas is 20 ppm, the sensor sensitivity is 1.07, which is 0.14 less than that when the concentration of aniline gas is 20 ppm, and the sensor sensitivity of the latter is 1.21. When the concentration of aniline gas is 90 ppm, the sensor sensitivity is 1.51, indicating good sensitivity. In Figure 10b, the sensor sensitivity varies with the concentration of ethanol gas. In general, the sensor sensitivity is relatively high when the concentration of ethanol gas is high. When the concentration of ethanol gas is 1.0%, the sensor sensitivity is 1.029, while when the concentration of ethanol gas is 2.0%, the sensor sensitivity is 1.046; When the concentration of ethanol gas is 3%, the sensor sensitivity is 1.05. The repeatability of the designed sensor is checked by selecting aniline and ethanol, and the relevant results are shown in Figure 11.

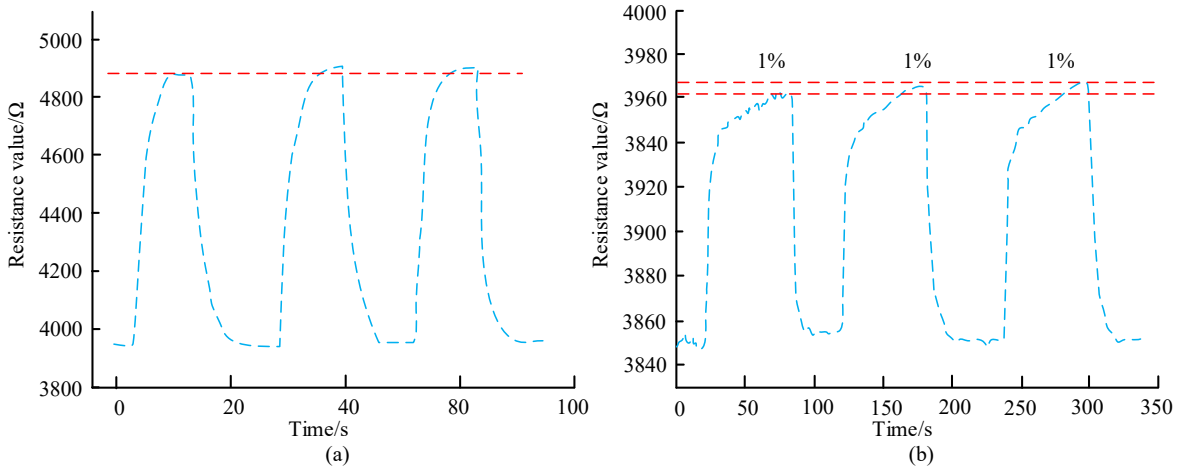

Figure 11. Sensor repeatability detection results. (**a**) Sensor repeatability for 50 ppm aniline. (**b**) Sensor repeatability for 1% ethanol.

In Figure 11a, when 50 ppm aniline gas is repeatedly introduced three times, there is a certain deviation in the measured resistance values of the sensor. When the time is 10 s, the sensor resistance value is 4880 Ω, which is 440 Ω smaller than when the time is 30 s. After three measurements, it is known that the repeatability error is 2.6%. In Figure 11b, by repeatedly applying 1% ethanol three times, the changes in the resistance values of the three sensors are basically the same, and after the gas is released, the resistance values of the second and third sensors can be restored to the initial resistance values. According to the calculation, the repeatability error is 4.2%. This illustrates that the sensor designed in

the study has good repeatability and stable performance. Under relevant conditions and doping ratio, four array sensor units A1, A2, B1, and B2 were prepared, their detection performance was analyzed for different concentrations, and their consistency was studied, as shown in Figure 12.

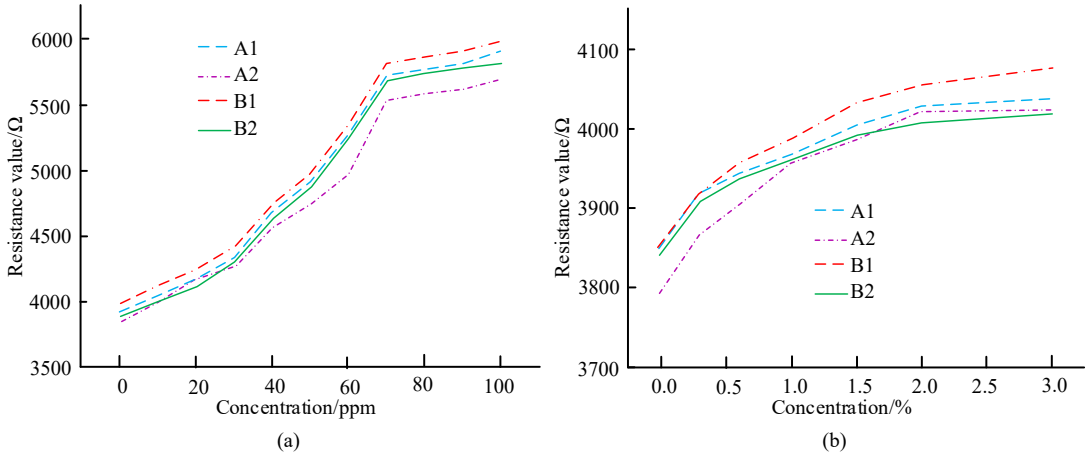

Figure 12. Curve of resistance value changing with the concentration of aniline gas and ethanol gas. (**a**) Curve of Resistance Value Changing with Aniline Gas Concentration. (**b**) Curve of Resistance Value Changing with Ethanol Gas Concentration.

In Figure 12a,b, according to the curves of different sensing units, A1, B1 and B2 have good consistency, while A2 has poor consistency, and the trend of their corresponding curves is different from the other three sensing units. The reason for this situation may be due to the significant difference in thickness and uniformity of the sensitive material film on the sensing unit caused by manual coating of sensitive materials, resulting in poor consistency, but overall good consistency. The image characteristics of the designed sensor were analyzed, and the R and B components of the four units A1, B1, and other gases with different concentrations were obtained, as shown in Table 3.

Table 3. The R and B components of each unit in gases of different concentrations.

Gas	Concentration	A1		A2		B1		B2	
		R1	B1	R2	B2	R3	B3	R4	B4
Ethanol	20 ppm	57.69	5.96	77.49	18.91	77.22	13.68	89.18	12.47
	40 ppm	61.52	6.40	75.39	20.42	67.03	17.89	94.09	17.03
	60 ppm	61.84	4.53	82.21	21.28	61.08	11.94	80.51	19.01
	80 ppm	62.78	7.07	88.32	22.86	72.33	13.98	81.84	11.79
Formaldehyde	20 ppm	79.78	5.59	73.48	12.09	37.06	8.66	36.56	11.28
	40 ppm	69.92	6.29	77.88	6.92	35.38	11.74	43.32	12.66
	60 ppm	69.66	6.38	66.08	9.40	32.86	6.53	31.83	9.32
	80 ppm	70.08	8.05	76.87	9.87	36.93	9.21	45.77	10.77
Aniline	20 ppm	72.58	12.33	58.28	12.53	57.37	14.47	64.34	16.55
	40 ppm	73.79	12.32	59.81	13.57	58.72	15.83	59.23	18.58
	60 ppm	75.78	13.05	65.33	12.51	63.18	13.28	68.39	15.57
	80 ppm	73.76	15.04	52.90	11.28	59.82	15.57	75.12	14.26
Toluene	20 ppm	55.31	7.51	47.89	6.88	43.47	12.08	56.58	9.01
	40 ppm	58.39	10.59	48.30	12.69	46.58	16.27	55.86	7.87
	60 ppm	49.16	8.57	49.83	8.96	44.30	13.53	54.20	8.66
	80 ppm	50.20	10.07	56.97	7.93	41.94	9.62	55.17	10.78

In Table 3, the component differences of gases with different concentrations in different units are different. In Unit A1, the R1 component difference of 20 ppm formaldehyde is 79.78, which is 6.3 greater than that of Unit A2 at this concentration. The R1 component

difference of the latter is 73.48; The R1 component difference of 60 ppm toluene is 49.16, while its B1 component difference is 8.57. Comparing the R and B components of the same unit in the same gas concentration illustrates that the difference between the R component and the B component is smaller. On the basis of the data in Table 3, four different sensors were used to obtain the differences between two R and B components, for a total of eight feature vectors. SPSS 19.0 software was selected to perform clustering analysis on the detected data, and the relevant clustering analysis diagram is shown in Figure 13 [22].

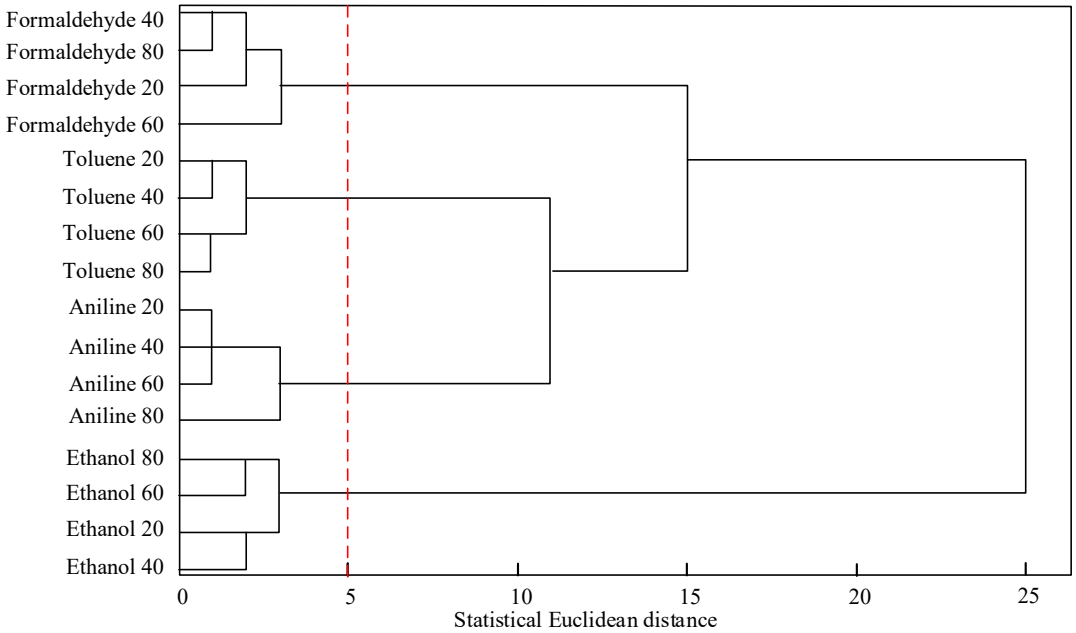

Figure 13. Correlation clustering analysis chart.

In Figure 13, formaldehyde 40 represents formaldehyde with a concentration of 40 ppm, aniline 80 represents aniline with a concentration of 80 ppm, and other gases are similar. Figure 12 reveals that the same gas with different concentrations is clustered together. According to the principle of "elbow rule", change the number of clusters and calculate the cost function for different clusters to obtain a correlation aggregation coefficient graph. Based on the elbow points in the graph, select the corresponding number of clusters as the optimal number of clusters. Therefore, the optimal number of classes was determined during clustering. In view of the maximum degree of distortion between the number of classes and the clustering coefficient, the optimal number of clusters is determined to be four, and the threshold of Euclidean distance is set to five. This can effectively identify four types of gases, including toluene and formaldehyde.

5. Conclusions

To detect VOCs in enclosed environments, this study combines MEMS technology to manufacture a stacked MEMS gas sensor. It utilizes porphyrin-sensitive materials doped with carbon nanotube materials to improve the initial resistance of the sensor and conduct gas sensitivity testing of the sensor. The results show that compared with the micro hotplate 1, the micro hotplate 2 has uniform temperature distribution, low power consumption and more stable mechanical properties. The temperature in the active area of Micro Hot Plate 2 is mostly around 102 °C, with a difference of 2.21 °C between the highest and lowest temperatures, while the temperature difference in the active area of Micro Hot Plate 1 is 4.632 °C. The maximum deformation of micro hot plate 2 is 3.7×10^{-2} μm. Compared with the other two types of porphyrin materials, porphyrin zinc/carbon nanocomposites have better thermal stability. Before 358 °C, the weight of the porphyrin material remained basically unchanged, and it began to absorb heat from 358 °C. Before 171.7 °C, the weight

loss of porphyrin zinc material is 5%. Before 464.4 °C, the porphyrin zinc/carbon nanocomposites lost 6% of their weight. In the gas sensitivity performance testing of the designed sensor, the sensor has good response recovery characteristics, sensitivity, and repeatability. The response time and recovery time to aniline gas are 33 s and 23 s, respectively. When the concentration of aniline gas is 90 ppm, the sensor sensitivity is 1.51. When 1% ethanol is repeatedly injected three times, the repeatability error of the sensor is 4.2%. In the analysis of sensor image characteristics, it can effectively classify VOC gases. It demonstrates that the stacked MEMS gas sensor studied and designed is effective. In the future, the range of sensor applications can be expanded and applied to more types of VOC gas detection.

Author Contributions: G.W., J.W., J.D. and X.Z. collected the samples. G.W. and J.W. analysed the data. J.D. and X.Z. conducted the experiments and analysed the results. All authors discussed the results and wrote the manuscript. All authors have read and agreed to the published version of the manuscript.

Funding: This research received no external funding.

Data Availability Statement: All data generated or analysed during this study are included in this published article.

Conflicts of Interest: The authors declare no conflict of interest.

References

1. Meng, Z.; Tong, B.; Shen, L.; Xu, L.; Sheng, Z. Au nanoparticle modified single-crystalline p-type $LaRhO_3/SrTiO_3$ heterostructure for high performing VOCs sensor. *Ceram. Int.* **2020**, *46*, 22140–22145. [CrossRef]
2. Wang, C.; Yu, H.Y.; Miao, Z. Interface growth of PANI-ZnO Nanohybrids on a self-formed grapefruit peel aerogel to construct a quick self-restored gas sensor. *ACS Sustain. Chem. Eng.* **2022**, *10*, 6573–6583. [CrossRef]
3. Wang, X.; Zhang, P.; Xu, Q.; Guo, C.; Zhang, D.; Lu, C.; Liu, R. Enantioselective synthesis of nitrogen-nitrogen biaryl atropisomers via copper-catalyzed friedel-crafts alkylation reaction. *J. Am. Chem. Soc.* **2021**, *143*, 15005–15010. [CrossRef]
4. Chen, D.; Wang, Q.; Li, Y.; Li, Y.; Zhou, H.; Fan, Y. A general linear free energy relationship for predicting partition coefficients of neutral organic compounds. *Chemosphere* **2020**, *247*, 125869. [CrossRef] [PubMed]
5. Mishra, J.P.; Singh, K.; Chaudhary, H. A hybrid noise removal algorithm for MEMS sensor. *Mater. Today Proc.* **2021**, *1*, 5791–5796. [CrossRef]
6. Paszek, K.; Grzechca, D.; Tomczyk, M.; Marciniak, A. UWB Positioning System with the Support of MEMS Sensors for Indoor and Outdoor Environment. *J. Commun.* **2020**, *15*, 511–518. [CrossRef]
7. Jiang, W.; Zhang, W.; Shi, J.; Lyu, Y.; Chen, H. Globally asymptotic stable attitude estimation with application to MEMS sensors. *Xibei Gongye Daxue Xuebao/J. Northwestern Polytech. Univ.* **2020**, *38*, 550–557. [CrossRef]
8. Fu, W.; Sun, L.; Cao, H.; Chen, L.; Zhou, M.; Shen, S.; Zhuang, S. Qualitative and quantitative recognition of volatile organic compounds in their liquid phase based on terahertz microfluidic EIT meta-sensors. *IEEE Sens. J.* **2023**, *23*, 12775–12784. [CrossRef]
9. Acharyya, S.; Nag, S.; Kimbahune, S.; Ghose, A.; Pal, A.; Guha, P. Selective discrimination of VOCs applying gas sensing kinetic analysis over a metal oxide-based chemiresistive gas sensor. *ACS Sens.* **2021**, *6*, 2218–2224. [CrossRef]
10. Fedorov, F.S.; Solomatin, M.A.; Uhlemann, M.; Oswald, S.; Kolosov, D.A.; Morozov, A.; Varezhnikov, A.S.; Ivanov, M.A.; Grebenko, A.K.; Sommer, M. Quasi-2D Co3O4 nanoflakes as an efficient gas sensor versus alcohol VOCs. *J. Mater. Chem. A* **2020**, *8*, 7214–7228. [CrossRef]
11. Srinivasan, P.; Samanta, S.; Krishnakumar, A.; Rayappan, J.B.B.; Kailasam, K. Insights into g-C3N4 as a chemi-resistive gas sensor for VOCs and humidity a review of the state of the art and recent advancements. *J. Mater. Chem. A Mater. Energy Sustain.* **2021**, *17*, 10612–10651. [CrossRef]
12. Xing, X.; Yang, Y.; Yan ZHu, Y.; Zou, T.; Wang, Z.; Wang, Y. CdO-Ag-ZnO nanocomposites with hierarchically porous structure for effective VOCs gas-sensing properties–ScienceDirect. *Ceram. Int.* **2019**, *45*, 4322–4334. [CrossRef]
13. Bouricha, B.; Sekrafi, T.; Labidi, A.; Dridil, C. VOCs identification method based on one single ZnTTP sensor. *IEEE Sens. J.* **2022**, *9*, 9242–9250. [CrossRef]
14. Osawa, Y.; Hata, S.; Hori, M.; Dohi, T. Analysis of blood pressure pulse wave and electrocardiogram waveforms measured by a wearable device with MEMS sensors. *Sens. Mater. Int. J. Sens. Technol.* **2021**, *33*, 1063–1072. [CrossRef]
15. Liao, M. Progress in semiconductor diamond photodetectors and MEMS sensors. *Funct. Diam.* **2022**, *1*, 29–46. [CrossRef]
16. Nuzzo, F.D.; Brunelli, D.; Polonelli, T.; Benini, L. Structural health monitoring system with narrowband IoT and MEMS sensors. *IEEE Sens. J.* **2021**, *21*, 16371–16380. [CrossRef]
17. Burger, T.; Winkler, C.; Dalfen, I.; Slugovc, C.; Borisov, S.M. Porphyrin based metal–organic frameworks: Highly sensitive materials for optical sensing of oxygen in gas phase. *J. Mater. Chem. C* **2021**, *9*, 17099–17112. [CrossRef]
18. Yang, X.; Cui, J.; Xue, K.; Fu, Y.; Yang, H. Thermal conductivity and thermoelectric properties in 3D macroscopic pure carbon nanotube materials. *Nanotechnol. Rev.* **2021**, *10*, 178–186. [CrossRef]

19. Zhang, L.; Qin, D.; Feng, J.; Tang, T.; Cheng, H. Rapid quantitative detection of luteolin using an electrochemical sensor based on electrospinning of carbon nanofibers doped with single-walled carbon nanoangles. *Anal. Methods* **2023**, *15*, 3073–3083. [CrossRef]
20. Singu, B.S.; Sobhy, E.; Yoon, K.R. Carbon Nanotube–Manganese oxide nanorods hybrid composites for high-performance supercapacitor materials. *J. Ind. Eng. Chem.* **2021**, *97*, 239–249. [CrossRef]
21. Wan, Q.; Huang, C.; Hou, Z.; Jiang, H.; Wang, L. Organophotoelectrochemical silylation cyclization for the synthesis of silylated 3-CF3-2-oxindoles. *Org. Chem. Front.* **2023**, *10*, 3585–3590. [CrossRef]
22. Smarandache, F. Plithogeny, plithogenic set, logic, probability and statistics: A short review. *J. Comput. Cogn. Eng.* **2022**, *1*, 47–50. [CrossRef]